Accepted Manuscript

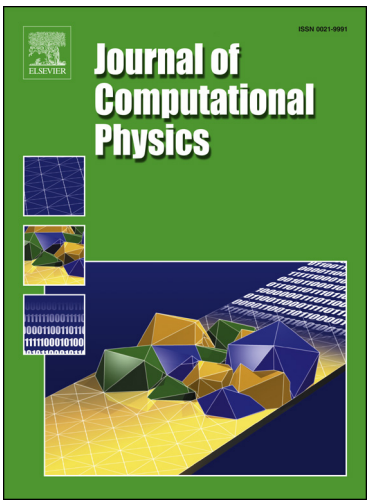

High-order well-balanced finite volume schemes for the Euler equations with gravitation

L. Grosheintz-Laval, R. Käppeli

PII: S0021-9991(18)30736-8
DOI: https://doi.org/10.1016/j.jcp.2018.11.018
Reference: YJCPH 8371

To appear in: *Journal of Computational Physics*

Received date: 15 June 2018
Revised date: 9 November 2018
Accepted date: 10 November 2018

Please cite this article in press as: L. Grosheintz-Laval, R. Käppeli, High-order well-balanced finite volume schemes for the Euler equations with gravitation, *J. Comput. Phys.* (2018), https://doi.org/10.1016/j.jcp.2018.11.018

Highlights

- An arbitrarily high-order well-balanced finite volume scheme for Euler equations with gravity is presented.
- The presented scheme can handle arbitrary gravitational potentials and equations of state.
- The discrete preserved state is not imposed a priori.
- Several numerical experiments demonstrate that the scheme preserves the hydrostatic equilibrium to machine precision and resolves general flows with high-order of accuracy. Furthermore, the scheme is robust.

High-order well-balanced finite volume schemes for the Euler equations with gravitation

L. Grosheintz-Laval[a,*], R. Käppeli[a]

[a] *Seminar for Applied Mathematics (SAM), Department of Mathematics, ETH Zürich, CH-8092 Zürich, Switzerland*

Abstract

A high-order well-balanced scheme for the Euler equations with gravitation is presented. The scheme is able to preserve a spatially high-order accurate discrete representation of isentropic hydrostatic equilibria. It is based on a novel local hydrostatic reconstruction, which, in combination with any standard high-order accurate reconstruction procedure, achieves genuine high-order accuracy for smooth solutions close or away from equilibrium. The resulting scheme is very simple and can be implemented into any existing finite volume code with minimal effort. Moreover, the scheme is not tied to any particular form of the equation of state, which is crucial for example in astrophysical applications. Several numerical experiments were performed with a third-order accurate reconstruction. They demonstrate the robustness and high-order accuracy of the scheme nearby and out of hydrostatic equilibrium.

Keywords: Numerical methods, Hydrodynamics, Source terms, Well-balanced schemes

1. Introduction

A multitude of interesting physical phenomena are modeled by the Euler equations with gravitational source terms. Applications range from the study of atmospheric phenomena, such as numerical weather prediction and climate modeling, to the numerical simulation of the climate of exoplanets, convection in stars and core-collapse supernova explosions. The Euler equations with gravitational source terms express the conservation of mass, momentum and energy:

$$\frac{\partial \rho}{\partial t} + \nabla \cdot (\rho \boldsymbol{v}) = 0 \tag{1.1}$$

$$\frac{\partial \rho \boldsymbol{v}}{\partial t} + \nabla \cdot (\rho \boldsymbol{v} \otimes \boldsymbol{v}) + \nabla p = -\rho \nabla \phi \tag{1.2}$$

$$\frac{\partial E}{\partial t} + \nabla \cdot (\boldsymbol{v}\,(E + p)) = -\rho \boldsymbol{v} \nabla \phi. \tag{1.3}$$

Here ρ is the mass density, $\boldsymbol{v}$ the velocity and

$$E = \rho e + \frac{\rho}{2} v^2 \tag{1.4}$$

*Corresponding author
Email address: luc.grosheintz@sam.math.ethz.ch (L. Grosheintz-Laval)

the total fluid energy density being the sum of internal and kinetic energy densities. The pressure p is related to the density and specific internal energy through an equation of state $p = p(\rho, e)$.

The source terms on the right-hand side of the momentum and energy equations model the effect of the gravitational forces on the fluid. They are dictated by the variation of the gravitational potential ϕ, which can either be a given function or, in the case of self-gravity, be determined by the Poisson equation

$$\nabla^2 \phi = 4\pi G \rho, \tag{1.5}$$

where G is the gravitational constant.

In many physically relevant applications, such as the ones named above, (parts of) the flow of interest may be realized close to hydrostatic equilibrium

$$\nabla p = -\rho \nabla \phi. \tag{1.6}$$

As a matter of fact, the numerical simulation of near equilibrium flows is challenging for standard finite volume methods. The reason for this is that these methods may in general not satisfy a discrete equivalent of the equilibrium. Thus such states are not preserved exactly but are solely approximated with an error proportional to the truncation error of the scheme. So if the interest relies in the simulation of small perturbations on top of a hydrostatic equilibrium, the numerical resolution has to be increased to the point that the truncation errors do not obscure these small perturbations. This may result in prohibitively high computational costs, especially in several space dimensions.

A design principle to overcome the challenge was introduced by Greenberg and Leroux [1] leading to the concept of so-called well-balanced schemes. In these schemes, a discrete equivalent of the equilibrium is exactly satisfied. Therefore, they possess the ability to maintain discrete equilibrium states down to machine precision and are capable of resolving small equilibrium perturbations effectively. Many well-balanced schemes have been designed, especially for the shallow water equations with non-trivial bottom topography, see e.g. [2, 3, 4] and references therein. An extensive review on well-balanced schemes for many different applications is also given in the book by Gosse [5].

Well-balanced schemes for the Euler equations with gravitation have received a considerable amount of attention in the recent literature. First, LeVeque and Bale [6] have applied the quasi-steady wave-propagation algorithm [2] to the Euler equations with gravity. Few years later, Botta et al. [7] designed a well-balanced finite volume scheme for numerical weather prediction applications. More recently, several well-balanced finite volume [8, 9, 10, 11, 12, 13, 14, 15, 16, 17] , finite difference [18, 19] and discontinuous Galerkin [20, 21, 22] schemes have been presented. Magnetohydrostatic steady state preserving well-balanced finite volume schemes were devised in [23]. To the best of our knowledge, many of the mentioned schemes are at most second-order accurate and only [18, 20, 21, 19, 22, 24] go to higher orders.

In fact, equation (1.6) only specifies a mechanical equilibrium. In order to fully characterize the equilibrium a thermal variable, such as the specific entropy s or the temperature T, needs to be supplemented. As a concrete astrophysically relevant example of a stationary state we consider the case of constant entropy. The relevant thermodynamic relation for isentropic hydrostatic equilibrium is

$$\mathrm{d}h = T\,\mathrm{d}s + \frac{\mathrm{d}p}{\rho}, \tag{1.7}$$

where h is the specific enthalpy

$$h = e + \frac{p}{\rho}, \tag{1.8}$$

T the temperature and s the specific entropy. Then we can write (1.6) for the isentropic case ($\mathrm{d}s = 0$) as

$$\frac{1}{\rho}\nabla p = \nabla h = -\nabla\phi. \tag{1.9}$$

The last equation can then be trivially integrated to obtain

$$h + \phi = const. \tag{1.10}$$

In [9] this equilibrium was used to build a second-order accurate well-balanced finite volume scheme. Along the same lines, well-balanced schemes for isothermal hydrostatic equilibrium can be constructed [15]. In the latter case, the relevant thermodynamic potential is the Gibbs free energy. More generally, the presented approach can be applied to barotropic fluids characterized by the fact that the density is a funcion of pressure only. In that case, the expression

$$\Theta = \int \frac{\mathrm{d}p}{\rho}$$

is integrable and the hydrostatic equilibrium takes the form

$$\Theta + \phi = const.$$

We note that the isentropic and the isothermal as well as the polytropic equilibrium [11, 22] fall into this category. However, in the following we focus on the isentropic case. Many interesting physical phenomena involve steady convection that takes place near the isentropic state. For example athmospheric convection on Earth and exoplanets [25], convection in stars and neutron stars [26, 27].

In this paper, we extend the well-balanced finite volume schemes [9] beyond second-order accuracy. The scheme possesses the following novel features:

- An arbitrarily high-order accurate local hydrostatic profile is constructed based on the equilibrium (1.10).
- An arbitrarly high-order equilibrium preserving reconstruction is designed on the basis of any standard high-order reconstruction procedure.
- A well-balanced source term discretization is built from the equilibrium preserving reconstruction.

Furthermore, the scheme has the following properties:

- It is well-balanced for any consistent numerical flux, which allows a straightforward implementation within any standard finite volume method.
- It is well-balanced for multi-dimensional hydrostatic equilibria.
- It is not tied to any particular equation of state such as the ideal gas law. This is important, especially for astrophysical applications.

The resulting scheme is high-order accurate for flows far and close to an equilibrium state. It is well-balanced in that it preserves exactly (down to machine precision) a high-order approximation of equilibria of the form Eq. (1.10).

The rest of the paper is structured as follows: the well-balanced finite volume scheme is presented in section 2. Extensive numerical results are presented in section 3 and conclusions are provided in section 4.

2. Numerical Method

2.1. One-dimensional scheme

We first consider the Euler equations with gravitation (1.1–3) in one space dimension and write them in the following compact form

$$\frac{\partial \boldsymbol{u}}{\partial t} + \frac{\partial \boldsymbol{f}}{\partial x} = \boldsymbol{s} \tag{2.1}$$

with

$$\boldsymbol{u} = \begin{bmatrix} \rho \\ \rho v_x \\ E \end{bmatrix}, \quad \boldsymbol{f} = \begin{bmatrix} \rho v_x \\ \rho v_x^2 + p \\ (E + p) v_x \end{bmatrix} \quad \text{and} \quad \boldsymbol{s} = - \begin{bmatrix} 0 \\ \rho \\ \rho v_x \end{bmatrix} \frac{\partial \phi}{\partial x}, \tag{2.2}$$

where $\boldsymbol{u}$, $\boldsymbol{f}$ and $\boldsymbol{s}$ are the vectors of conserved variables, fluxes and source terms. An equation of state (EoS) $p = p(\rho, e)$ relates the pressure to the density ρ and specific internal energy e (or any other thermodynamic quantity such as specific entropy s or temperature T). For example, a simple EoS is provided by the ideal gas law

$$p = \rho e (\gamma - 1), \tag{2.3}$$

where γ is the ratio of specific heats. We stress that the well-balanced scheme derived below is not tied to any particular form of EoS, which is crucial especially in astrophysical applications.

In the next section we will briefly describe a standard high-order finite-volume discretization and it's core components in order to fix the notation. The following sections will then describe our novel well-balanced scheme in detail.

2.1.1. Finite-volume discretization

For the numerical approximation of (2.1), the spatial domain of interest is discretized by a number of cells or finite volumes $I_i = [x_{i-1/2}, x_{i+1/2}]$. Here $x_{i\pm1/2}$ denotes the left and right cell interface, respectively, and $x_i = (x_{i-1/2} + x_{i+1/2})/2$ the cell center of I_i. For ease of presentation, we assume a regular cell size $\Delta x = x_{i+1/2} - x_{i-1/2}$. Nevertheless, varying cell sizes can easily be accommodated for.

A one-dimensional semi-discrete finite volume scheme is then given by

$$\frac{\mathrm{d}\overline{\boldsymbol{U}}_i}{\mathrm{d}t} = \mathcal{L}(\overline{\boldsymbol{U}}) = -\frac{1}{\Delta x} \left(\boldsymbol{F}_{i+1/2} - \boldsymbol{F}_{i-1/2} \right) + \overline{\boldsymbol{S}}_i, \tag{2.4}$$

where $\overline{\boldsymbol{U}}_i = \overline{\boldsymbol{U}}_i(t)$ denotes the approximate cell average of the conserved variables in cell I_i at time t. It approximates the exact cell average $\overline{\boldsymbol{u}}_i = \overline{\boldsymbol{u}}_i(t)$ of the true solution $\boldsymbol{u}(t, x)$ at time t:

$$\overline{\boldsymbol{U}}_i(t) \approx \overline{\boldsymbol{u}}_i(t) = \frac{1}{\Delta x} \int_{I_i} \boldsymbol{u}(t, x) \, \mathrm{d}x. \tag{2.5}$$

In the following, a quantity with an overbar indicates a cell average while a quantity without indicates a point value. By $\overline{\boldsymbol{S}}_i(t)$ is denoted the approximate cell average of the true source terms at time t:

$$\overline{\boldsymbol{S}}_i(t) \approx \overline{\boldsymbol{s}}_i(t) = \frac{1}{\Delta x} \int_{I_i} \boldsymbol{s}(\boldsymbol{u}, \frac{\partial \phi}{\partial x}) \, \mathrm{d}x. \tag{2.6}$$

Note that we have suppressed the time dependence of the gravitational potential since we are mainly concerned with flows close to hydrostatic equilibrium and for ease of notation.

Numerical flux. The numerical flux is obtained by solving (approximately) the Riemann problem at cell interfaces

$$\boldsymbol{F}_{i+1/2} = \mathcal{F}(\boldsymbol{U}_{i+1/2-}, \boldsymbol{U}_{i+1/2+}), \tag{2.7}$$

where the point values $\boldsymbol{U}_{i+1/2\mp}$ are the cell interface extrapolated conserved variables and $\mathcal{F}$ is a consistent, i.e. $\mathcal{F}(\boldsymbol{u}, \boldsymbol{u}) = \boldsymbol{f}(\boldsymbol{u})$, and Lipschitz continuous numerical flux function.

Below, we will make use of the HLLC approximate Riemann solver with simple wave speed estimates from [28, 29], but our well-balanced scheme is independent of this particular choice.

Reconstruction. The purpose of a reconstruction procedure $\mathcal{R}$ is to compute accurate point values of the approximate solution $\boldsymbol{U}_i(t, x)$ within each cell from the cell averages $\overline{\boldsymbol{U}}$. We denote such a reconstruction procedure, which recovers a r-th order accurate point value of a quantity c at location x within cell I_i from the cell averages $\overline{c}$, by

$$c_i(x) = \mathcal{R}(x; \{\overline{c}_k\}_{k \in S_i}). \tag{2.8}$$

Here S_i is the stencil for the reconstruction procedure for cell I_i, i.e. S_i is a finite set of neighbors of I_i.

The values of the conserved variables extrapolated to the interface are then given by

$$\boldsymbol{U}_{i+1/2-} = \boldsymbol{U}_i(t, x_{i+1/2}) = \mathcal{R}\left(x_{i+1/2}; \{\overline{\boldsymbol{U}}_k\}_{k \in S_i}\right) \quad \text{and} \quad \boldsymbol{U}_{i+1/2+} = \boldsymbol{U}_{i+1}(t, x_{i+1/2}) = \mathcal{R}\left(x_{i+1/2}; \{\overline{\boldsymbol{U}}_k\}_{k \in S_{i+1}}\right).$$

Many such reconstruction procedures have been developed and a non-exhaustive list includes the Total Variation Diminishing (TVD) methods (see e.g. [30, 31]), the Piecewise-Parabolic Method (PPM) [32], Essentially Non-Oscillatory (ENO) (see e.g. [33]), Weighted ENO (WENO) (see e.g. [34] and references therein) and Central WENO (CWENO) methods (see e.g. [35] and references therein).

In the scheme derived below we will use a CWENO type reconstruction procedure. This choice is motivated by the fact that CWENO provides an entire reconstruction polynomial defined everywhere in a cell, which is convenient for the evaluation of the gravitational source terms. However, our scheme is independent of this particular choice. The only requirement is that the reconstruction can compute point values at all quadrature points in the interior and on the boundary of the computational cell. Therefore, the scheme can also be applied to WENO type reconstructions, if one takes care to treat the possibly appearing negative weights properly (we refer to [34] and references therein for details).

Source term discretization. The approximate cell average of the source term $\overline{\boldsymbol{S}}_i$ is obtained by numerical integration. Let Q_i denote a q-th order accurate quadrature rule over cell I_i. Then the cell average of the source term is approximated by

$$\overline{\boldsymbol{S}}_i = \frac{1}{\Delta x} Q_i\left(\boldsymbol{s}(\boldsymbol{U}, \frac{\partial \phi}{\partial x})\right) = \frac{1}{\Delta x} \sum_{\alpha=1}^{N_q} \omega_\alpha \, \boldsymbol{s}\left(\boldsymbol{U}_i(t, x_{i,\alpha}), \frac{\partial \phi}{\partial x}(x_{i,\alpha})\right), \tag{2.9}$$

where the $x_{i,\alpha} \in I_i$ and ω_α denote the N_q quadrature nodes and weights of Q_i, respectively. For example, the two-point Gauss-Legendre quadrature rule can be used, which is the choice we will make below. The latter choice will be sufficient to achieve the third-order accuracy seeked in Section 3. The point values of the conserved variables at the quadrature nodes $\boldsymbol{U}_i(t, x_{i,\alpha})$ are obtained by the reconstruction procedure:

$$\boldsymbol{U}_i(t, x_{i,\alpha}) = \mathcal{R}\left(x_{i,\alpha}; \{\overline{\boldsymbol{U}}_k\}_{k \in S_i}\right). \tag{2.10}$$

If the gravitational potential is known analytically, it can be evaluated directly at the quadrature nodes. If the gravitational potential is only known at discrete points, then an interpolation of ϕ and finite difference of $\nabla\phi$ can be used instead. Both the interpolation and the finite difference need to be at least as accurate as the chosen design order.

Temporal discretization. The temporal domain of interest $[0, T]$ is discretized into time steps $\Delta t = t^{n+1} - t^n$, where the superscript n labels the different time levels. For the temporal integration, the high-order strong stability-preserving Runge-Kutta (SSP-RK) schemes [36] can be used. In particular, we use the third-order SSP-RK method for the numerical results presented in this paper

$$\begin{aligned} \overline{\boldsymbol{U}}_i^{(1)} &= \overline{\boldsymbol{U}}_i^n + \Delta t \mathcal{L}(\overline{\boldsymbol{U}}^n) \\ \overline{\boldsymbol{U}}_i^{(2)} &= \frac{3}{4}\overline{\boldsymbol{U}}_i^n + \frac{1}{4}\left(\overline{\boldsymbol{U}}_i^{(1)} + \Delta t \mathcal{L}(\overline{\boldsymbol{U}}^{(1)})\right) \\ \overline{\boldsymbol{U}}_i^{n+1} &= \frac{1}{3}\overline{\boldsymbol{U}}_i^n + \frac{2}{3}\left(\overline{\boldsymbol{U}}_i^{(2)} + \Delta t \mathcal{L}(\overline{\boldsymbol{U}}^{(2)})\right), \end{aligned} \tag{2.11}$$

where $\mathcal{L}$ denotes the spatial discretization operator from (2.4). Furthermore, the time step Δt is required to fulfill the CFL condition for finite volume methods [36, 37] with a CFL number specified in the numerical experiments.

This concludes the description of a standard high-order finite volume scheme for the Euler equations. We refer to the excellent books available in the literature for detailed derivations, e.g. [38, 39, 40, 2]. However, a standard reconstruction procedure and source term discretization will in general not preserve a discrete equivalent of hydrostatic equilibrium. In order to achieve this, we need the ingredients presented in the following two sections 2.1.2 and 2.1.3.

2.1.2. Local hydrostatic reconstruction

The local hydrostatic reconstruction consists of two parts. First, within each cell a high-order accurate equilibrium profile that is consistent with the cell-averaged conserved variables is determined. Second, the cell's equilibrium profile is extrapolated to neighboring cells to perform a high-order accurate reconstruction of the equilibrium perturbation.

We begin by describing how the local high-order accurate equilibrium profile is determined. Within the i-th cell I_i, we define a subcell equilibrium reconstruction of the specific enthalpy $h_{eq,i}(x)$ by assuming (1.10) as

$$h_{eq,i}(x) = h_{0,i} + \phi_i - \phi(x). \tag{2.12}$$

Here $h_{0,i} = h_{eq,i}(x_i)$ and $\phi_i = \phi(x_i)$ are point values of the specific enthalpy and the gravitational potential at the cell center, respectively. In the following, we assume that the gravitational potential can be evaluated anywhere, either because it is a given function or obtained by a suitable interpolation.

In combination with the (assumed constant) equilibrium entropy $s_{0,i}$ in cell I_i, the equilibrium density $\rho_{eq,i}(x)$ and internal energy density $\rho e_{eq,i}(x)$ profiles can be computed through the EoS:

$$\rho_{eq,i}(x) = \rho(h_{eq,i}(x), s_{0,i}) \quad \text{and} \quad \rho e_{eq,i}(x) = \rho e(h_{eq,i}(x), s_{0,i}).$$

The computational complexity of this computation depends strongly on the functional form of the EoS. For the ideal gas case, explicit expressions are given in Appendix A.

We note that the equilibrium specific enthalpy $h_{0,i}$ and entropy $s_{0,i}$ are not specified so far. In order to fix $h_{0,i}$ and $s_{0,i}$, we demand that the equilibrium density and internal energy density profiles agree up to the desired order of accuracy with their respective cell average in cell I_i. Hence, we seek $h_{0,i}$ and $s_{0,i}$ such that

$$\begin{aligned} \overline{\rho}_i &= \frac{1}{\Delta x} Q_i(\ \rho_{eq,i}) = \frac{1}{\Delta x} \sum_{\alpha=1}^{N_q} \omega_\alpha\, \rho(h_{eq,i}(x_{i,\alpha}), s_{0,i}) \\ \overline{\rho e}_i &= \frac{1}{\Delta x} Q_i(\rho e_{eq,i}) = \frac{1}{\Delta x} \sum_{\alpha=1}^{N_q} \omega_\alpha\, \rho e(h_{eq,i}(x_{i,\alpha}), s_{0,i}), \end{aligned} \tag{2.13}$$

where Q_i denotes the previously introduced q-th order accurate quadrature rule over cell I_i. In the above expression, an estimate of the cell average of the internal energy density $\overline{\rho e}_i$ is needed. We simply estimate it directly from the cell-averaged conserved variables by

$$\overline{\rho e}_i = \overline{E}_i - \frac{1}{2}\frac{\overline{\rho v}_{x,i}^2}{\overline{\rho}_i}, \tag{2.14}$$

which is exact at equilibrium ($v_x \equiv 0$).

Note that, in general, (2.13) represents a nonlinear system of two equations in the equilibrium specific enthalpy at cell center $h_{0,i}$ and the (constant) specific entropy $s_{0,i}$. This system must be solved iteratively, e.g. with Newton's method. In practice, the iterative process is started from the specific entropy and enthalpy computed from the cell-averaged conserved variables $\overline{\boldsymbol{U}}_i$. The cost of this iterative process is mitigated by the fact that it is local to each cell and the initial guess is a spatially second order accurate estimate, i.e. a very small two-by-two system of equations must be solved, independently, in every cell starting from a good initial guess. For the ideal gas law, the system can be reduced to a single nonlinear equation for which existence and uniqueness of the solution can be guaranteed under very weak requirements. This is shown in Appendix A.

Once $h_{0,i}$ and $s_{0,i}$ have been fixed, we have the following high-order accurate representation of the equilibrium in cell I_i:

$$\boldsymbol{U}_{eq,i}(x) = \begin{bmatrix} \rho_{eq,i}(x) \\ 0 \\ \rho e_{eq,i}(x) \end{bmatrix}. \tag{2.15}$$

Next we develop the high-order equilibrium preserving reconstruction procedure. The idea is to decompose the solution into an equilibrium and a (possibly large) perturbation part. Within cell I_i, the equilibrium part is simply given by the previously derived equilibrium profile $\boldsymbol{U}_{eq,i}(x)$. The perturbation part is obtained by applying the standard reconstruction $\mathcal{R}$ procedure on the equilibrium perturbation cell averages

$$\delta\boldsymbol{U}_i(x) = \mathcal{R}\left(x; \{\overline{\boldsymbol{U}}_k - \boldsymbol{Q}_k(\boldsymbol{U}_{eq,i})\}_{k\in S_i}\right), \tag{2.16}$$

which results in a $\min(q, r)$-th order accurate representation of the equilibrium perturbation in cell I_i. Note that the equilibrium perturbation cell average in cell I_k is obtained by taking the difference between the actual cell average $\overline{\boldsymbol{U}}_k$ in cell I_k and the cell average of the equilibrium profile $\boldsymbol{U}_{eq,i}(x)$ in cell I_k. The latter is evaluated by applying the I_k cell's quadrature rule $\boldsymbol{Q}_k$ to $\boldsymbol{U}_{eq,i}(x)$.

The full equilibrium preserving reconstruction $\mathcal{W}$ is then obtained by simply adding the equilibrium profile to the perturbation

$$\boldsymbol{U}_i(x) = \mathcal{W}(x; \{\overline{\boldsymbol{U}}_k\}_{k\in S_i}) = \boldsymbol{U}_{eq,i}(x) + \delta\boldsymbol{U}_i(x). \tag{2.17}$$

We observe that, by construction, this reconstruction will preserve any equilibrium of the form (1.10), since the perturbation $\delta\boldsymbol{U}_i(x)$ vanishes under these conditions.

The reason this is high-order is that any function can be written as some other function plus the difference, i.e. $f = g + (f - g)$. Clearly, this difference $\delta f = f - g$ can be reconstructed from the cell-averages of the difference, i.e. $\delta f(x) \approx \mathcal{R}(x; \{\bar{f}_k - \bar{g}_k\}_{k\in S})$. Therefore, the well-balanced reconstruction procedure (2.17) is high-order accurate, for any smooth function $\boldsymbol{U}_{eq,i}(x)$ (which takes the role of g in the previous argument).

2.1.3. Well-balanced source term discretization

For the momentum source discretization, we use the previous splitting of the cell I_i's density $\rho_i(x)$ into equilibrium $\rho_{eq,i}(x)$ and perturbation $\delta\rho_i(x)$ as

$$S_{\rho v,i}(x) = -\rho_i(x)\frac{\partial\phi}{\partial x}(x) = -\left(\rho_{eq,i}(x) + \delta\rho_i(x)\right)\frac{\partial\phi}{\partial x}(x) = -\rho_{eq,i}(x)\frac{\partial\phi}{\partial x}(x) - \delta\rho_i(x)\frac{\partial\phi}{\partial x}(x),$$

which is clearly a pointwise $\min(q, r)$-th order accurate approximation of the true source term. However, a straightforward numerical integration will not result in a well-balanced scheme. Instead, we use the fact that for the equilibrium profiles we have

$$\frac{\partial p_{eq,i}}{\partial x} = -\rho_{eq,i}\frac{\partial\phi}{\partial x}$$

by construction. As a result, the equilibrium part of the momentum source term can be trivially integrated and numerical integration is only applied to the perturbation part:

$$\overline{S}_{\rho v,i} = \frac{p_{eq,i}(x_{i+1/2}) - p_{eq,i}(x_{i-1/2})}{\Delta x} - \frac{1}{\Delta x}\mathcal{Q}_i\left(\delta\rho_i\frac{\partial\phi}{\partial x}\right). \tag{2.18}$$

We remark that a similar approach of splitting the source term into an equilibrium and perturbation part was devised by Li and Xing [22] in a discontinuous Galerkin context. Since we are only concerned with stationary equilibria, the energy source term $\overline{S}_{E,i}$ discretization is left unchanged from (2.9).

We summarize the developed high-order well-balanced finite volume scheme in the following theorem:

Theorem 2.1 *Consider the scheme* (2.4) *with a consistent and Lipschitz continuous numerical flux $\mathcal{F}$, a r-th order accurate spatial reconstruction procedure $\mathcal{R}$, a q-th order accurate quadrature rule $\mathcal{Q}$, the hydrostatic reconstruction $\mathcal{W}$* (2.17) *and the gravitational source term $\mathcal{S}$* (2.9) *(with* (2.18)*).*

This scheme has the following properties:

(i) *The scheme is consistent with* (2.1) *and it is* $\min(q, r)$*-th order accurate in space (for smooth solutions).*

(ii) *The scheme is well-balanced and preserves the discrete hydrostatic equilibrium given by* (1.10) *and* $v_x = 0$ *exactly.*

Proof (i) The consistency and formal order of accuracy of the scheme is straightforward.

(ii) Let the hydrostatic equilibrium (1.10) be characterized by the constant specific entropy s and specific enthalpy profile $h_{eq}(x)$. The equilibrium conserved variables are then given by $u_{eq}(x) = [\rho(h_{eq}(x), s), 0, \rho e(h_{eq}(x), s)]^T$ and let $\boldsymbol{U}_i(0) = \frac{1}{\Delta x}\mathcal{Q}_i\left(\boldsymbol{u}_{eq}\right)$ be the discrete initial conditions. Then the iterative process for solving (2.13) will, in each cell, find the local equilibrium $h_{0,i} = h_{eq}(x_i)$ and $s_{0,i} = s$. We prove this fact for ideal gases in Appendix A. Therefore, in every cell $\delta\boldsymbol{U}_i(x) = \mathcal{R}(x; \{0\}_{k\in S_i}) = 0$. Hence, we have $\boldsymbol{U}_{i+1/2-} = \boldsymbol{U}_{i+1/2+}$ and by consistency of the numerical flux $\boldsymbol{F}_{i+1/2} = \boldsymbol{f}(\boldsymbol{U}_{i+1/2-}) = [0, p_{eq}(x_{i+1/2}), 0]^T$. Likewise, by definition (2.18) the cell-averaged source term becomes $\overline{\boldsymbol{S}}_i = \frac{1}{\Delta x}[0, p_{eq}(x_{i+1/2}) - p_{eq}(x_{i-1/2}), 0]^T$. By plugging the above expressions for the numerical flux and source term into the semi-discrete finite volume scheme (2.4) we get

$$\frac{\mathrm{d}\overline{\boldsymbol{U}}_i}{\mathrm{d}t} = \mathcal{L}(\overline{\boldsymbol{U}}) = -\frac{1}{\Delta x}\left(\boldsymbol{F}_{i+1/2} - \boldsymbol{F}_{i-1/2}\right) + \overline{\boldsymbol{S}}_i = 0$$

Thus the scheme is well-balanced as claimed. ■

Remark 2.2 *The presented scheme reduces to the second-order accurate scheme presented in [9] by setting the quadrature rule $\mathcal{Q}$ to the midpoint rule and the reconstruction procedure $\mathcal{R}$ to piecewise linear.*

2.2. Extension to several space dimensions

We now describe the extension of our well-balanced scheme for hydrostatic equilibrium to the multi-dimensional case. For ease of presentation, we describe it for two dimensions and the extension to three dimensions is straightforward. As in the one-dimensional case, we briefly introduce a standard high-order finite volume scheme and then detail the well-balanced scheme.

The two-dimensional Euler equations with gravity in Cartesian coordinates are given by

$$\frac{\partial \boldsymbol{u}}{\partial t} + \frac{\partial \boldsymbol{f}}{\partial x} + \frac{\partial \boldsymbol{g}}{\partial y} = \boldsymbol{s} \tag{2.19}$$

with

$$\boldsymbol{u} = \begin{bmatrix} \rho \\ \rho v_x \\ \rho v_y \\ E \end{bmatrix}, \quad \boldsymbol{f} = \begin{bmatrix} \rho v_x \\ \rho v_x^2 + p \\ \rho v_y v_x \\ (E+p) v_x \end{bmatrix}, \quad \boldsymbol{g} = \begin{bmatrix} \rho v_y \\ \rho v_x v_y \\ \rho v_y^2 + p \\ (E+p) v_y \end{bmatrix} \quad \text{and} \quad \boldsymbol{s} = \boldsymbol{s}_x + \boldsymbol{s}_y = \begin{bmatrix} 0 \\ -\rho \\ 0 \\ -\rho v_x \end{bmatrix} \frac{\partial \phi}{\partial x} + \begin{bmatrix} 0 \\ 0 \\ -\rho \\ -\rho v_y \end{bmatrix} \frac{\partial \phi}{\partial y}, \tag{2.20}$$

where $\boldsymbol{u}$ is the vector of conserved variables, $\boldsymbol{f}$ and $\boldsymbol{g}$ the fluxes in x- and y-direction, and $\boldsymbol{s}$ the gravitational source terms.

We consider a rectangular spatial domain $\Omega = [x_{\min}, x_{\max}] \times [y_{\min}, y_{\max}]$ discretized uniformly (for ease of presentation) by N_x and N_y cells or finite volumes in x- and y-direction, respectively. The cells are labeled by $I_{i,j} = I_i \times I_j = [x_{i-1/2}, x_{i+1/2}] \times [y_{j-1/2}, y_{j+1/2}]$ and the constant cell sizes by $\Delta x = x_{i+1/2} - x_{i-1/2}$ and $\Delta y = y_{j+1/2} - y_{j-1/2}$. We denote the cell centers by $x_i = (x_{i-1/2} + x_{i+1/2})/2$ and $y_j = (y_{j-1/2} + y_{j+1/2})/2$. Integrals of some quantity c over the cell faces are approximated by q-th order accurate quadrature rules as

$$\begin{aligned} Q_{i\pm1/2,j}(c) &= \sum_{\beta=1}^{N_q} \omega_\beta \, c(x_{i\pm1/2}, y_{j,\beta}) \approx \int_{I_j} c(x_{i\pm1/2}, y) \, \mathrm{d}y \\ Q_{i,j\pm1/2}(c) &= \sum_{\alpha=1}^{N_q} \omega_\alpha \, c(x_{i,\alpha}, y_{j\pm1/2}) \approx \int_{I_i} c(x, y_{i\pm1/2}) \, \mathrm{d}x, \end{aligned} \tag{2.21}$$

where the $x_{i,\alpha} \in I_i$, $y_{j,\beta} \in I_j$ and ω_α, ω_β denote the N_q quadrature nodes and weights, respectively. Likewise, integrals over the cells are approximated by

$$Q_{i,j}(c) = \sum_{\alpha=1}^{N_q} \sum_{\beta=1}^{N_q} \omega_\alpha \omega_\beta \, c(x_{i,\alpha}, y_{j,\beta}) \approx \int_{I_{i,j}} c(x, y) \, \mathrm{d}x \, \mathrm{d}y. \tag{2.22}$$

A semi-discrete finite volume scheme for the numerical approximation of (2.19) then takes the following form

$$\frac{\mathrm{d}\overline{\boldsymbol{U}}_{i,j}}{\mathrm{d}t} = \mathcal{L}(\overline{\boldsymbol{U}}) = -\frac{1}{\Delta x}\left(\boldsymbol{F}_{i+1/2,j} - \boldsymbol{F}_{i-1/2,j}\right) - \frac{1}{\Delta y}\left(\boldsymbol{G}_{i,j+1/2} - \boldsymbol{G}_{i,j-1/2}\right) + \overline{\boldsymbol{S}}_{i,j}, \tag{2.23}$$

where $\overline{\boldsymbol{U}}_{i,j}$ denotes the approximate cell averages of the conserved variables, $\boldsymbol{F}_{i\pm1/2,j}$ and $\boldsymbol{G}_{i,j\pm1/2}$ the facial averages of the fluxes through the cell boundary and $\overline{\boldsymbol{S}}_{i,j}$ the cell averages of the source term. The fluxes are obtained by applying the above quadrature rules along the cell boundary to the numerical flux formulas $\mathcal{F}$ and $\mathcal{G}$ in respective direction:

$$\begin{aligned} \boldsymbol{F}_{i+1/2,j} &= \frac{1}{\Delta y} Q_{i+1/2,j}\left(\mathcal{F}(\boldsymbol{U}_{i,j}, \boldsymbol{U}_{i+1,j})\right) \\ \boldsymbol{G}_{i,j+1/2} &= \frac{1}{\Delta x} Q_{i,j+1/2}\left(\mathcal{G}(\boldsymbol{U}_{i,j}, \boldsymbol{U}_{i,j+1})\right), \end{aligned} \tag{2.24}$$

where $\boldsymbol{U}_{i,j} = \boldsymbol{U}_{i,j}(x, y)$ is a suitable reconstruction to be defined in detail at a later point. Similarly, the source term is obtained by quadrature over the cell

$$\overline{\boldsymbol{S}}_{i,j} = \frac{1}{\Delta x \Delta y} \boldsymbol{Q}_{i,j}(\boldsymbol{s}(\boldsymbol{U}, \nabla \phi)). \tag{2.25}$$

In the evaluation of the quadrature rules, a r-th reconstruction procedure $\mathcal{R}$ is used to obtain pointwise representations of the solution from the cell-averaged conserved variables:

$$\boldsymbol{U}_{i,j}(x, y) = \mathcal{R}\left(x, y; \left\{\overline{\boldsymbol{U}}_{k,l}\right\}_{(k,l)\in S_{i,j}}\right). \tag{2.26}$$

Here $S_{i,j}$ is the stencil of the reconstruction for cell $I_{i,j}$. Many such reconstruction procedures have been developed in the literature and we refer to the references previously mentioned in section 2.1.1.

As in the one-dimensional case, we need two ingredients to construct our well-balanced scheme. The first is a high-order equilibrium preserving reconstruction and the second is a well-balanced discretization of the momentum source terms.

Let us begin with the description of the first ingredient and consider cell $I_{i,j}$. Then the high-order equilibrium preserving reconstruction $\mathcal{W}$ takes the following form

$$\boldsymbol{U}_{i,j}(x, y) = \mathcal{W}\left(x, y; \left\{\overline{\boldsymbol{U}}_{k,l}\right\}_{(k,l)\in S_{i,j}}\right) = \boldsymbol{U}_{eq,i,j}(x, y) + \delta \boldsymbol{U}_{i,j}(x, y), \tag{2.27}$$

which again separates the solution into an equilibrium $\boldsymbol{U}_{eq,i,j}$ and a (possibly large) perturbation $\delta \boldsymbol{U}_{i,j}$.

The equilibrium profile is built from (1.10), which is indeed also valid in more than one dimensions. Hence, we construct the local equilibrium profile in cell $I_{i,j}$ by

$$h_{eq,i,j}(x, y) = h_{0,i,j} + \phi_{i,j} - \phi(x, y), \tag{2.28}$$

where $h_{0,i,j} = h_{eq,i,j}(x_i, y_j)$ and $\phi_{i,j} = \phi(x_i, y_j)$ are the point values of the specific enthalpy and the gravitational potential at cell center, respectively. Given the (constant) equilibrium entropy $s_{0,i,j}$, the equilibrium profiles of density $\rho_{eq,i,j}$ and internal energy density $\rho e_{eq,i,j}$ can be computed through the EoS.

The equilibrium enthalpy at cell center $h_{0,i,j}$ and the (constant) entropy $s_{0,i,j}$ are again fixed by demanding agreement with the local cell averages up to the desired order of accuracy:

$$\begin{aligned} \overline{\rho}_{i,j} &= \frac{1}{\Delta x \Delta y} \boldsymbol{Q}_{i,j}(\rho_{eq,i,j}) \\ \overline{\rho e}_{i,j} &= \frac{1}{\Delta x \Delta y} \boldsymbol{Q}_{i,j}(\rho e_{eq,i,j}). \end{aligned} \tag{2.29}$$

Here $\overline{\rho e}_{i,j}$ is the cell average of the internal energy density, which we estimate simply from the cell-averaged conserved variables by

$$\overline{\rho e}_{i,j} = \overline{E}_{i,j} - \frac{1}{2\overline{\rho}_{i,j}} \left(\overline{\rho v}^2_{x,i,j} + \overline{\rho v}^2_{y,i,j}\right), \tag{2.30}$$

The latter estimate is again exact at equilibrium. As in the one-dimensional case, these equations represent, in general, a nonlinear system of two equations in the equilibrium specific enthalpy at cell center $h_{0,i,j}$ and the (constant) specific entropy $s_{0,i,j}$. Their resolution proceeds as in the one-dimensional case. In the end, we have the following equilibrium profile

$$\boldsymbol{U}_{eq,i,j}(x, y) = \begin{bmatrix} \rho_{eq,i,j}(x, y) \\ 0 \\ 0 \\ \rho e_{eq,i,j}(x, y) \end{bmatrix}. \tag{2.31}$$

The perturbation part is reconstructed as in the one-dimensional case by

$$\delta \boldsymbol{U}_{i,j}(x,y) = \mathcal{R}\left(x, y; \left\{\overline{\boldsymbol{U}}_{k,l} - Q_{k,l}(\boldsymbol{U}_{eq,i,j})\right\}_{(k,l)\in S_{i,j}}\right). \tag{2.32}$$

This simply extrapolates the cell's local equilibrium profile, computes equilibrium cell averages by numerical integration, and uses the standard reconstruction procedure to obtain a high-order representation of the perturbation.

We observe that the reconstruction procedure (2.27) preserves the equilibrium by construction, since $\delta \boldsymbol{U}_{i,j}$ vanishes, and it is $\min(q,r)$-th order accurate in and away from equilibrium (for sufficiently smooth solutions).

As in the one-dimensional case, only the momentum source terms need to be modified. The well-balanced momentum source terms are simply obtained on a dimension-by-dimension basis

$$\begin{aligned}
\overline{S}_{\rho v_x,i,j} &= \frac{1}{\Delta x}\left(Q_{i+1/2,j}(p_{eq,i,j}) - Q_{i-1/2,j}(p_{eq,i,j})\right) - \frac{1}{\Delta x \Delta y} Q_{i,j}\left(\delta\rho_{i,j}\frac{\partial \phi}{\partial x}\right) \\
\overline{S}_{\rho v_y,i,j} &= \frac{1}{\Delta y}\left(Q_{i,j+1/2}(p_{eq,i,j}) - Q_{i,j-1/2}(p_{eq,i,j})\right) - \frac{1}{\Delta x \Delta y} Q_{i,j}\left(\delta\rho_{i,j}\frac{\partial \phi}{\partial y}\right).
\end{aligned} \tag{2.33}$$

This completes the description of the two-dimensional well-balanced scheme for hydrostatic equilibrium and its properties are summarized in the corollary below:

Corollary 2.3 *Consider the scheme* (2.23) *with consistent and Lipschitz continuous numerical fluxes $\mathcal{F}$ and $\mathcal{G}$, a r-th order accurate spatial reconstruction procedure $\mathcal{R}$, a q-th order accurate quadrature rule Q, the hydrostatic reconstruction $\mathcal{W}$* (2.27) *and the gravitational source term $\mathcal{S}$* (2.25) *(with* (2.33)*).*

This scheme has the following properties:

(i) *The scheme is consistent with* (2.19) *and it is* $\min(q,r)$*-th order accurate in space (for smooth solutions).*

(ii) *The scheme is well-balanced and preserves the discrete hydrostatic equilibrium given by* (1.10) *and* $v_x = v_y = 0$ *exactly.*

Proof The proof follows directly by applying theorem 2.1 dimension-by-dimension. ■

3. Numerical Experiments

In this section we assess the performance of our well-balanced scheme on a series of numerical experiments. For comparison, we also present results obtained with a standard (unbalanced) base scheme. The fully-discrete finite volume base scheme consists of

- the temporally third-order accurate SSP-RK scheme for time integration (see [36]),
- the spatially third-order accurate CWENO3 [41] reconstruction procedure $\mathcal{R}$,
- the spatially fourth-order accurate two-point Gauss-Legendre quadrature rule for Q.

Overall, the chosen component results in a scheme that is third-order accurate in space and time. This scheme is conditionally stable under the usual CFL condition. We use a CFL number of $C_{\mathrm{CFL}} = 0.85$. In the following, we will refer to this scheme as the unbalanced scheme. The well-balanced scheme is built with the

same base components, but uses the well-balanced reconstruction procedure and source term computation as outlined in the previous section.

Below, all the initial conditions will be given in functional form $\boldsymbol{u}_0(\boldsymbol{x})$. The discrete initial conditions are obtained simply by quadrature, i.e.

$$\overline{\boldsymbol{U}}_i^0 = \boldsymbol{Q}_i(\boldsymbol{u}_0), \quad \overline{\boldsymbol{U}}_{i,j}^0 = \boldsymbol{Q}_{i,j}(\boldsymbol{u}_0) \tag{3.1}$$

in the one- and two-dimensional case, respectively. It is important to notice that the well-balancing only requires that the initial conditions are obtained by the exact same quadrature rule used in the numerical scheme. Therefore, showing that the initial conditions are well-balanced will immediately imply that the preserved discrete state is a high-order accurate approximation of the exact equilibrium, simply because the discrete initial conditions are nothing else than a high-order quadrature of the exact equilibrium.

We will be using three distinct notions of "error". The first error is the usual L^1-error

$$err_1(q) := \sum_i \Delta x \, |\overline{q}_i - \overline{q}_{ref,i}|, \tag{3.2}$$

where q is any scalar variable of interest, e.g. $q = \rho, p, v, \ldots$. Furthermore, $\overline{q}_{ref,i}$ is computed by down-sampling a high-resolution reference solution or, where available, a highly accurate quadrature of an analytic solution. A subtlety is that even in a well-balanced scheme the err_1 of a discrete preserved state is not, in general, zero. This is simply because $\boldsymbol{U}_i^0$ is a high-order approximation of the exact cell-average of the initial conditions and is therefore in general not exact. However, the important fact is that the err_1 does not grow in time for the well-balanced scheme.

To answer the question of how big the error of a perturbation δq from equilibrium is, we define the L^1-error of δq as

$$err_1(\delta q) := \sum_i \Delta x \, |(\overline{q}_i - \boldsymbol{Q}_i(q_{eq})) - \delta\overline{q}_{ref,i}| \tag{3.3}$$

where q_{eq} is the background equilibrium profile and $\delta\overline{q}_{ref,i}$ is the cell-average of the perturbation in a reference solution. This measures the error of the perturbation from numerical equilibrium. This is subtly different than the error of the perturbation from the exact equilibrium. The difference is that $err_1(\delta q)$ conveniently uses the quadrature rule used in the finite volume method to compute the average of the equilibrium profile, i.e. $\boldsymbol{Q}_{i,j}q_{eq}$. Therefore, for equilibria, a well-balanced scheme should have zero $err_1(\delta q)$, but may have non-zero $err_1(q)$.

When computing the $err_1(\delta q)$ for hydrostatic equilibria, the reference solution $\boldsymbol{Q}_{i,j}(q_{eq})$ is known exactly, it's simply the initial condition. Therefore, $err_1(\delta q)$ can be computed at a greatly reduced computational cost by

$$err_{eq,1}(q) := \sum_i \Delta x |\overline{q}_i - \boldsymbol{Q}_i(q_{eq})| \tag{3.4}$$

In order to be clear about how the errors were computed we will make the distinction throughout the numerical experiments. Moreover, the above error measures readily generalize to the two-dimensional case.

To characterize a time scale on which a model reacts to perturbations of its equilibrium, we define the sound crossing time τ_{sound}

$$\tau_{\text{sound}} = 2 \int c_s^{-1} \mathrm{d}x, \tag{3.5}$$

where c_s denotes the speed of sound and the integral has to be taken over the extent of the stationary state of interest. The sound crossing time is basically the time in which a sound wave travels back and forth through the equilibrium.

We begin by several simple one- and two-dimensional numerical experiments employing the ideal gas EoS. The interested reader may readily reproduce these experiments in order to check his or her implementation. Finally, we demonstrate the performance of the scheme on a problem involving a complex multiphysics EoS.

3.1. One-dimensional Tests

We consider an isentropic hydrostatic atmosphere in a constant gravitational field. The gravitational potential is a linear function $\phi(x) = gx$ where g is the constant gravitational acceleration. The initial density and pressure profiles are then given by

$$\rho_0(x) = \left(\frac{1}{K} \frac{\gamma - 1}{\gamma} (h_0 - gx) \right)^{1/\gamma - 1}, \quad p_0(x) = K \rho_0(x)^\gamma + A \exp\left(-\frac{(x - 1/2)^2}{0.05^2} \right). \tag{3.6}$$

with the constants $g = 3.15$, $\gamma = 1.4$, $h_0 = 3.75$ and $K = 1$. The atmosphere's pressure is perturbed by a Gaussian bump of amplitude A. The velocity is set to zero everywhere.

The computational domain is set to $[0, L]$ with $L = 1$ and uniformly discretized by N cells, i.e. we set the cell size $\Delta x = L/N$, the cell interfaces $x_{i+1/2} = i\Delta x$ and the cell centers $x_i = (x_{i-1/2} + x_{i+1/2})/2$ for $i = 1, ..., N$. The following resolutions are used $N = 32, 64, 128, 256, 512, 1024$.

The boundary conditions are treated as follows. We extrapolate the local equilibrium from the last physical cell into the left and right ghost cells by

$$\begin{aligned} \overline{\boldsymbol{U}}_i &= Q_i(\boldsymbol{U}_{eq,1}) \quad \text{for} \quad i < 1 \\ \overline{\boldsymbol{U}}_i &= Q_i(\boldsymbol{U}_{eq,N}) \quad \text{for} \quad i > N. \end{aligned} \tag{3.7}$$

3.1.1. Well-balanced property

We first verify the well-balanced property of our scheme. For this we evolve the isentropic atmosphere in hydrostatic equilibrium without pressure perturbation, $A = 0$, up to time $t = 10$. This corresponds to roughly 6 sound crossing time ($\tau_{\text{sound}} = 1.6$). The numerical errors for the density at final time are shown in Table 1. The table clearly shows that the well-balanced scheme maintains the discrete stationary state to machine precision. Since the initial conditions are the two-point Gauss-Legendre quadrature of the exact equilibrium, this furthermore shows that the preserved state is a fourth order accurate approximation of the exact equilibrium. The unbalanced scheme produces large errors and is unable to maintain the hydrostatic equilibrium accurately.

3.1.2. Small pressure perturbation propagation

Next we add a small pressure perturbation to the isentropic atmosphere in order to examine the schemes ability to propagate small waves. The amplitude of the pressure perturbation is set to $A = 10^{-7}$, which generates one smooth wave propagating upwards and one downwards through atmosphere. As the waves propagate, they are modified by the density and pressure stratification of the atmosphere. We evolve the setup until time $t = 0.2$, shortly before the waves reach the boundaries.

The errors of the density perturbation $err_1(\delta\rho)$ are shown in Table 2. The density perturbation is the density at the final time minus the density of the unperturbed atmosphere. These errors were obtained on the basis of a reference solution computed by the unbalanced scheme with a high resolution $N = 32\,768$. We

N	CWENO3		CWENO3 wb	
	$err_{eq,1}(\rho)$	rate	$err_{eq,1}(\rho)$	rate
32	8.73×10^{-4}	–	9.85×10^{-16}	–
64	1.38×10^{-4}	2.66	3.96×10^{-15}	-2.01
128	1.21×10^{-5}	3.51	1.83×10^{-15}	1.11
256	1.21×10^{-6}	3.33	3.18×10^{-15}	-0.80
512	1.25×10^{-7}	3.27	4.49×10^{-15}	-0.50
1024	1.31×10^{-8}	3.25	8.34×10^{-15}	-0.89

Table 1: **Convergence data for the one-dimensional test Section 3.1.1 without perturbation. We show $err_{eq,1}(\rho)$ at $t = 10.0$. On the left we show the error for the unbalanced scheme and on the right hand side we shows the errors for the well-balanced scheme.**

observe that the errors of the well-balanced scheme are roughly four orders of magnitude smaller than the unbalanced scheme. The convergence rate of both the unbalanced and well-balanced reach the expected rate of three.

In Figure 1 the profile of the velocity and the pressure perturbation are shown at the final time for both the unbalanced (blue crosses) and well-balanced (red circle) schemes. The well-balanced solution is shown for $N = 64$. Even at this relatively low resolution the well-balanced scheme resolves the perturbation well. The errors of the unbalanced scheme for $N = 64$ are too large to be shown on the same plot. Instead we plot the solution of the unbalanced scheme at $N = 256$. Even at this increased resolution the perturbation is not approximated well and spurious drifts have developed during this short period of time.

N	CWENO3		CWENO3 wb	
	$err_1(\delta\rho)$	rate	$err_1(\delta\rho)$	rate
32	5.84×10^{-6}	–	3.02×10^{-9}	–
64	6.19×10^{-7}	3.24	8.12×10^{-10}	1.89
128	1.79×10^{-7}	1.79	1.34×10^{-10}	2.60
256	3.37×10^{-8}	2.41	1.84×10^{-11}	2.86
512	4.90×10^{-9}	2.78	2.40×10^{-12}	2.94
1024	6.24×10^{-10}	2.97	3.02×10^{-13}	2.99

Table 2: **Convergence data for the one-dimensional test Section 3.1.2 with the small perturbation $A = 10^{-7}$. We show the error of the density perturbation $err_1(\delta\rho)$ at $t = 0.2$. On the left we show the errors for the unbalanced scheme. The errors of the perturbation for the well-balanced scheme are given in the right hand side column.**

3.1.3. Large pressure perturbation propagation

For the purpose of testing that the well-balanced reconstruction does not destroy the robustness of the shock-capturing base scheme, we increase the pressure perturbation by several orders of magnitude to $A = 10$. This generates two strong waves quickly steepening into shock waves. The setup is evolved until time $t = 0.06$.

The plots of the velocity and pressure are shown in Figure 2. The two schemes are virtually indistinguishable by eye. In particular, the well-balanced scheme does not show any oscillations and performs equally

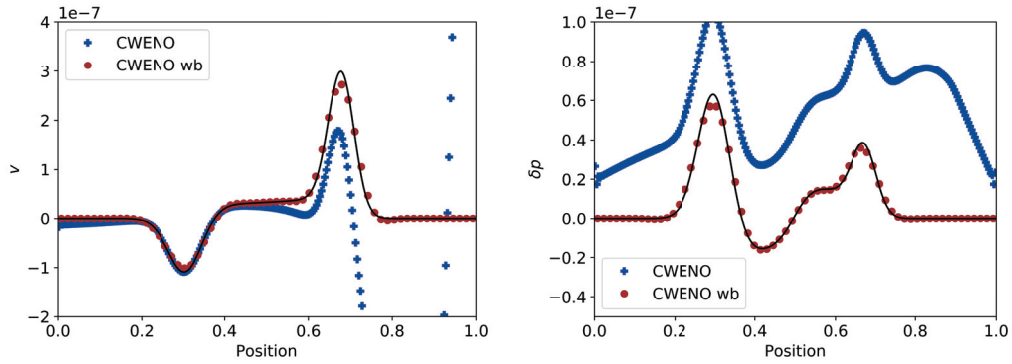

Figure 1: **Snapshot of the smooth test case, see Section 3.1.2. The simulation is performed with $N = 256$ and $N = 64$ cells for the unbalanced and well-balanced scheme respectively. It is run up to time $t = 0.2$. On the left we show the velocity, on the right the pressure perturbation. The error in the unbalanced scheme at $N = 64$ would be too big to be shown on the plot. The reference solution, plotted in black, is obtained by a high-resolution $N = 32\,768$ simulation using the unbalanced scheme.**

well as the underlying unbalanced scheme. The well-balancing has not adversely affected the performance of the scheme away from equilibrium.

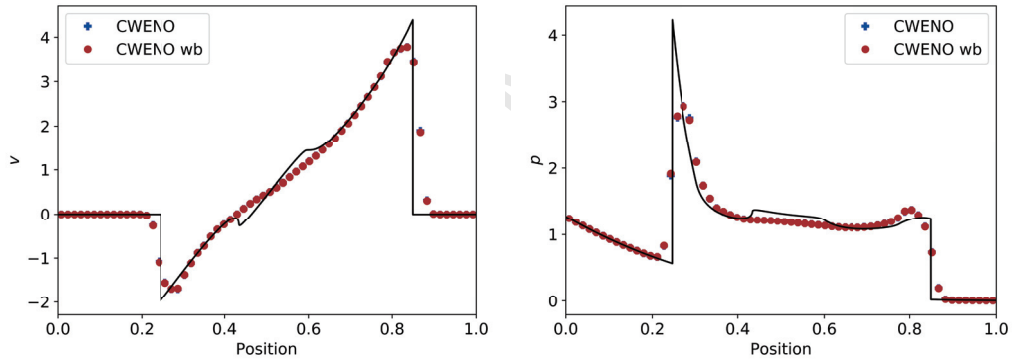

Figure 2: **Snapshot of one-dimensional test with large perturbation $A = 10$, see Section 3.1.3. The simulation is performed with $N = 64$ cells and run up to time $t = 0.06$. On the left the velocity is shown, on the right the pressure. The reference solution, plotted in black, is obtained by a high-resolution $N = 32\,768$ simulation using the unbalanced scheme.**

3.2. Two-dimensional polytrope

The following numerical experiment is a two-dimensional version of the one in [9]. This experiment simulates a so-called polytrope, which is a static configuration of an adiabatic gaseous sphere held together by self-gravitation. These model stars are constructed in spherical symmetry from hydrostatic equilibrium, Poisson's equation and the polytropic relation $p = K\rho^\gamma$, which can be combined into the so-called Lane-Emden equation (see e.g. [42]). The latter equation can be solved analytically for three values of the ratio of specific heats ($\gamma = 6/5, 2, \infty$).

As in [9] we use $\gamma = 2$. Then the density and pressure profiles are given by

$$\rho_0(r) = \rho_C \frac{\sin(\alpha r)}{\alpha r}, \quad p_0(r) = K\rho_0(r)^\gamma \tag{3.8}$$

where r is the radial coordinate, ρ_C is the central density of the polytrope and

$$\alpha = \sqrt{\frac{4\pi G}{2K}}. \tag{3.9}$$

The gravitational potential is given by

$$\phi(r) = -2K\rho_C \frac{\sin(\alpha r)}{\alpha r}. \tag{3.10}$$

In the following we set $K = G = \rho_C = 1$. Note that the polytrope (obviously) fulfills the equilibrium (1.10) for any $r \geq 0$.

We then discretize the problem on the computational domain $[-0.5, 0.5]^2$ by N^2 uniform cells for $N = 32, 64, 128, 256, 512, 1024$. The conserved variables are initialized by numerical integration of the conserved variables $\boldsymbol{u}_0(x, y) = [\rho_0(r), 0, 0, p_0(r)/(\gamma - 1)]^T$ where the radial coordinate is given by $r^2 = x^2 + y^2$. Note that the velocity is set to zero in the whole domain.

The boundary conditions are applied along the coordinates axes as in Section 3.1. In the corner boundaries (needed by the reconstruction procedure), we extrapolate the equilibrium from the relevant corner cell in the computational domain. For example, the ghost cell (i, j) in the upper right corner is set as follows

$$\overline{\boldsymbol{U}}_{i,j} = Q_{i,j}(\overline{\boldsymbol{U}}_{eq,N,N}). \tag{3.11}$$

The gravitational potential is simply given by the above analytical expression.

3.2.1. Well-balanced property

We begin by evolving the polytrope with the well-balanced and unbalanced scheme until time $t = 30$ which corresponds to roughly 35 sound-crossing times ($\tau_{sound} \approx 0.85$). The errors are shown in Table 3. **The unbalanced scheme converges at the expected rate, but even with 1024^2 cells, it has not reached round off. The well-balanced scheme is again shown to be in fact well-balanced. Like in the one-dimensional test, this implies that the preserved discrete state is fourth order accurate. This shows that the scheme also works in two-dimensions, even in cases where the gravity is non-constant and not grid-aligned.**

3.2.2. Perturbed polytrope

Next we add a perturbation to the equilibrium pressure of the polytrope as

$$p(r) = \left(1 + A\exp(-r^2/0.05^2)\right)\ p_0(r) \tag{3.12}$$

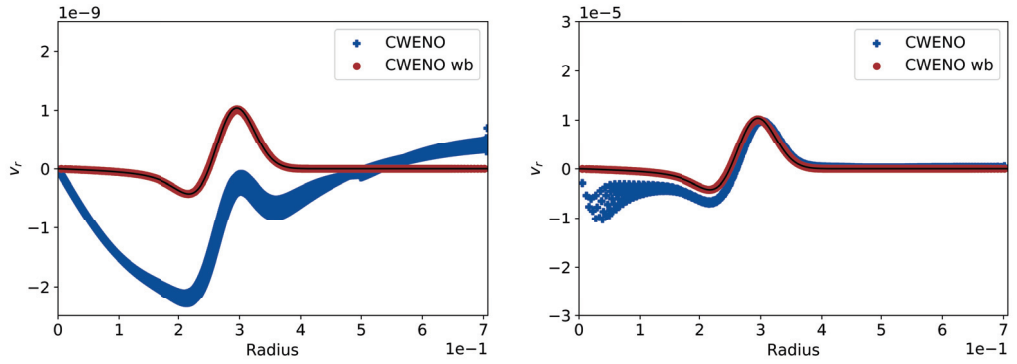

Figure 3: **Scatter plots of the two-dimensional polytrope, see Section 3.2.1 at time $t = 0.2$. The panel on the left shows the velocity for $A = 10^{-8}$. The panel on the right the corresponding plot for $A = 10^{-4}$. The resolution is generally $N = 128^2$, however, for the smallest perturbation, the errors of the unbalanced scheme at $N = 128$ exceed the limits of the plot. Therefore, for $A = 10^{-8}$, we plot the unbalanced scheme at $N = 1024^2$. The reference solution was computed with a one-dimensional finite volume code assuming cylindrical symmetry on $N = 32\,768$ cells.**

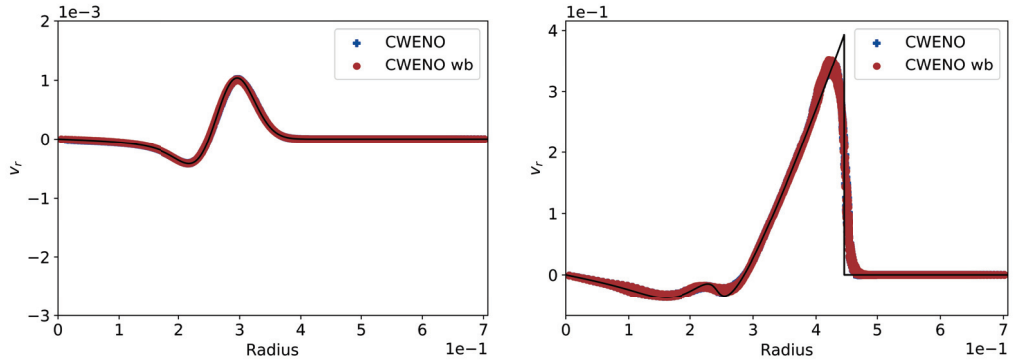

Figure 4: **Scatter plots of the two-dimensional polytrope, see Section 3.2.1. The simulation is performed with $N = 128^2$ cells and run up to time $t = 0.2$. The panel on the left shows the velocity for $A = 10^{-2}$, the one on the right for $A = 10$. The reference solution was computed with a one-dimensional finite volume code assuming cylindrical symmetry on $N = 32\,768$ cells.**

N	CWENO3		CWENO3 wb	
	$err_{eq,1}(\rho)$	rate	$err_{eq,1}(\rho)$	rate
32	1.57×10^{-3}	–	2.72×10^{-11}	–
64	1.85×10^{-4}	3.09	4.33×10^{-13}	5.97
128	2.22×10^{-5}	3.06	5.29×10^{-14}	3.03
256	2.66×10^{-6}	3.06	1.06×10^{-13}	-1.00
512	3.07×10^{-7}	3.12	2.04×10^{-13}	-0.95
1024	3.31×10^{-8}	3.21	3.94×10^{-13}	-0.95

Table 3: **Convergence data for the polytrope at rest, see Section 3.2.1. We show $err_{eq,1}(\rho)$ for the unbalanced scheme (left) and the well-balanced scheme (right).**

with three different amplitudes $A = 10^{-8}, 10^{-4}, 10^{-2}, 10$. The setup is evolved up to time $t = 0.2$ shortly before the excited waves reach the boundary of the computational domain.

The reference solution was computed with a one-dimensional second-order accurate finite volume scheme (assuming cylindrical symmetry) and resolution $N = 32\,768$.

For perturbations of size $A = 10^{-8}$ the well-balanced scheme clearly outperforms the unbalanced scheme (by at least four orders of magnitude). Scatter plots of the velocity and pressure perturbation are shown in Figure 3. At $N = 128^2$ the well-balanced scheme resolves the perturbation well and with no discernible scatter. Which is not trivial, since the radially symmetric solution is approximated on a uniform Cartesian grid which does not respect the radial symmetry.

At the next larger perturbation, $A = 10^{-4}$ the well-balanced scheme still outperforms the unbalanced scheme by a factor 10. Unlike the unbalanced scheme, the well-balanced scheme shows no scatter, as can be seen in Figure 3. Furthermore, once the perturbation has traveled away from the center of the domain, the solution returns back to equilibrium in the well-balanced scheme, but not in the unbalanced one. Both schemes converge at the expected rate.

The second largest perturbation, $A = 10^{-2}$, was chosen such that the perturbation is very well approximated by the unbalanced scheme, yet small enough to remain smooth. The aim is to show that away from equilibrium the well-balancing does not have a negative impact on the quality of the solution. This is confirmed in Figure 4 and Table 4.

For $A = 10$ both schemes perform equally well, both converge at first order and the errors differ by approximately one percent. Therefore, well-balancing has not affected the quality of the solution away from equilibrium. The scatter plot of the velocity and pressure is shown in Figure 4. Neither scheme shows any sign of spurious oscillations.

3.2.3. Blast waves

In order to further verify that our well-balanced scheme does not deteriorate the robustness and shock-capturing properties of the base scheme, we add to the polytrope several localized high pressure regions. To this end, we add the following pressure perturbation to the equilibrium polytrope

$$\delta p(\boldsymbol{x}) = 100 \sum_{i=1}^{6} \mathbf{1}_{B(\boldsymbol{x}_i, r)}(\boldsymbol{x}), \tag{3.13}$$

$A = 10^{-8}$	CWENO3		CWENO3 wb	
N	$err_1(\delta\rho)$	rate	$err_1(\delta\rho)$	rate
32	5.74×10^{-5}	–	5.01×10^{-11}	–
64	6.20×10^{-6}	3.21	1.58×10^{-11}	1.67
128	5.34×10^{-7}	3.54	2.74×10^{-12}	2.52
256	4.69×10^{-8}	3.51	3.71×10^{-13}	2.89
512	4.84×10^{-9}	3.28	5.34×10^{-14}	2.80
1024	5.67×10^{-10}	3.09	1.99×10^{-14}	1.42
$A = 10^{-4}$	CWENO3		CWENO3 wb	
N	$err_1(\delta\rho)$	rate	$err_1(\delta\rho)$	rate
32	5.76×10^{-5}	–	5.00×10^{-7}	–
64	6.27×10^{-6}	3.20	1.58×10^{-7}	1.66
128	5.46×10^{-7}	3.52	2.74×10^{-8}	2.52
256	4.70×10^{-8}	3.54	3.69×10^{-9}	2.89
512	4.84×10^{-9}	3.28	4.68×10^{-10}	2.98
1024	5.67×10^{-10}	3.09	5.87×10^{-11}	2.99
$A = 10^{-2}$	CWENO3		CWENO3 wb	
N	$err_1(\delta\rho)$	rate	$err_1(\delta\rho)$	rate
32	8.43×10^{-5}	–	5.50×10^{-5}	–
64	2.15×10^{-5}	1.97	1.79×10^{-5}	1.62
128	3.27×10^{-6}	2.72	2.84×10^{-6}	2.65
256	4.04×10^{-7}	3.02	3.72×10^{-7}	2.93
512	4.95×10^{-8}	3.03	4.68×10^{-8}	2.99
1024	6.14×10^{-9}	3.01	5.87×10^{-9}	3.00
$A = 10$	CWENO3		CWENO3 wb	
N	$err_1(\delta\rho)$	rate	$err_1(\delta\rho)$	rate
32	2.88×10^{-2}	–	2.98×10^{-2}	–
64	1.42×10^{-2}	1.02	1.46×10^{-2}	1.03
128	6.36×10^{-3}	1.16	6.46×10^{-3}	1.17
256	3.02×10^{-3}	1.08	3.05×10^{-3}	1.08
512	1.51×10^{-3}	1.00	1.51×10^{-3}	1.01
1024	7.69×10^{-4}	0.97	7.69×10^{-4}	0.97

Table 4: **Convergence data for the polytrope with perturbation. We show $err_1(\delta\rho)$ at $t = 0.2$ for the unbalanced (left) and well-balanced scheme (right) for different values of the amplitude A (indicated in the table). For the fourth table ($A = 10$) the smooth perturbation turns into a discontinuity and only first order convergence can be expected.**

where $B_{x,R} = \{x' \in \mathbb{R}^2 : \|x' - x\| < R\}$ denotes the open ball of radius R centered on x and $\mathbf{1}_B$ the indicator function for the set B, i.e.

$$\mathbf{1}_B(x) = \begin{cases} 1 & \text{if } x \in B, \\ 0 & \text{otherwise.} \end{cases}$$

We setup six "high pressure balls" with radii $R = 0.05$ and centers

$$x_1 = [-0.25, 0.3]^T,\ x_2 = [-0.15, 0.1]^T,\ x_3 = [0.025, 0.3]^T,\ x_4 = [0.025, 0.225]^T,$$
$$x_5 = x_6 = [0.1, -0.1]^T.$$

The velocity is set to zero everywhere. The initial conditions are shown in the upper panel of Figure 5.

We evolve the setup until time $t = 0.02$ with the well-balanced and unbalanced scheme at resolution $N = 128^2$ We show a snapshot at $t = 0.02$ in Figure 5. Even under these much more extreme conditions with non-trivial wave interactions, the well-balanced scheme is stable and by eye indistinguishable from the unbalanced scheme.

3.3. White Dwarf

The final numerical experiment assesses the performance of our well-balanced scheme on a astrophysically relevant problem involving a complex multiphysics EoS. We simulate the equilibrium and some perturbations of a model white dwarf. A white dwarf is the final evolutionary state of a star not massive enough to go through the final nuclear burning stages and become a neutron star or a black hole (see e.g. [27]).

This numerical experiment is a two-dimensional version of the one presented in [9]. Likewise, we use the publicly available Helmholtz EoS (see [43] for a detailed description and [44]). This EoS includes contributions of (photon) radiation, nuclei, electrons and positrons and is well adapted to large range of stellar environments. The radiation is treated as a blackbody in local thermal equilibrium and the nuclei are modeled by the ideal gas law. For computational efficiency, the electrons and positrons are treated in a tabular manner with a thermodynamically consistent interpolation procedure.

The publicly available EoS interface provides all relevant thermodynamic quantities given as input the temperature T, the density ρ and the composition (X_i, A_i, Z_i). Here X_i is the mass fraction, A_i the mass number and Z_i the atomic number of isotope i. As we evolve the Euler equations in conservative form, we therefore need to compute the temperature T corresponding to a given density ρ and specific internal energy e. For the equilibrium profile reconstruction, we need in addition the ability to recover the temperature T and the density ρ given the specific enthalpy h and entropy s. This is implemented with the help of root finding algorithms combining the Newton method for speed and the bisection method for robustness. We refer to Press et al. [45] for details.

The white dwarf model is fully characterized by specifying the central density, the chemical composition and the thermodynamic equilibrium. We set the central density $\rho = 2 \times 10^9$ g/cm^3 and temperature $T = 5 \times 10^8$ K. We assume a constant specific entropy and set the composition to half carbon ^{12}C and half oxygen ^{12}O. Then the model can be constructed by simple numerical integration of the self-gravitating hydrostatic equilibrium equations in spherical symmetry. We refer to [9] for the detailed procedure.

The one-dimensional white dwarf profile is then mapped onto the two-dimensional computational domain $[-L, L]^2$ with $L = 1 \times 10^8$ cm. The velocity is set to zero. The same hydrostatic extrapolation boundary conditions are used as in Section 3.2.

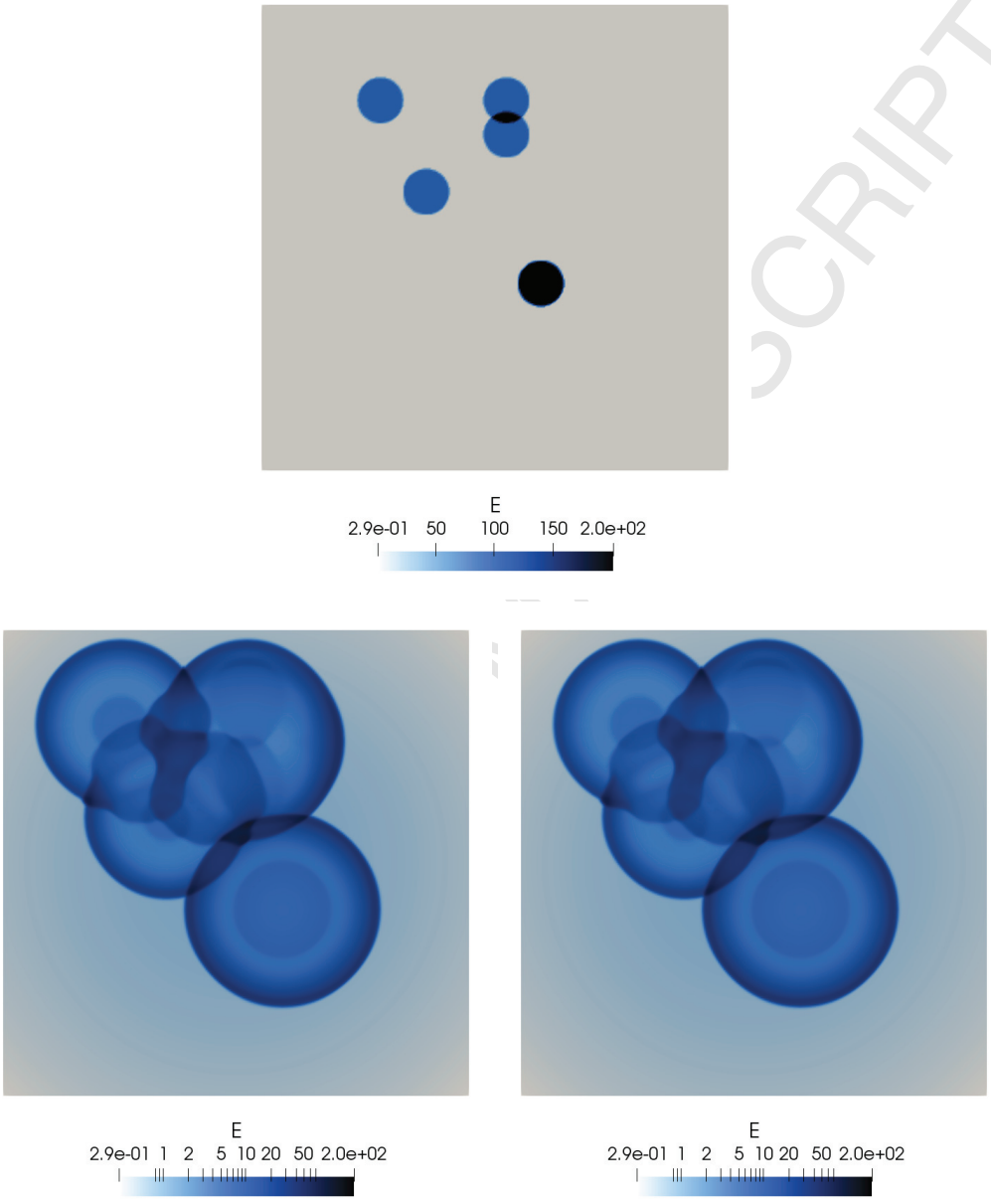

Figure 5: **Snapshot of the two dimensional blast waves, see Section 3.2.3. The upper image shows the initial total energy (on a linear scale). The remaining three plots show the total energy at** $t = 0.02$ **(on a logarithmic scale) for the unbalanced (bottom, left) and well-balanced (bottom, right) scheme.**

3.3.1. Well-balanced property

We evolve the hydrostatic equilibrium without perturbation on a grid with $N = 128^2$ cells until time $t = 1$ s. The unbalanced scheme has $err_{eq,1}(\rho)/\|\rho\|_\infty = 1.60 \times 10^{-5}$ and $err_{eq,1}(E)/\|E\|_\infty = 8.5 \times 10^{-6}$. The well-balanced scheme is confirmed to be exact up to machine precision, with errors of $err_{eq,1}(\rho)/\|\rho\|_\infty = 2.80 \times 10^{-15}$ and $err_{eq,1}(E)/\|E\|_\infty = 2.27 \times 10^{-15}$. Where $\|\rho\|_\infty = 2 \times 10^9$ g/cm^3 is the density and $\|E\|_\infty = 3.28 \times 10^{27}$ erg/cm^3 total energy at the center of the white dwarf. This shows that equation (2.29) can be solved numerically and the solution is effectively unique. If the iterative procedure were to find a different equilibrium in any cell, it would be very unlikely that the resulting scheme would be well-balanced.

3.3.2. Wave propagation

Next we add a small Gaussian pressure perturbation at the origin, i.e.

$$p_0(\boldsymbol{x}) = (1 + A \exp(-|\boldsymbol{x}|^2/2b^2))\, p_{eq}(\boldsymbol{x}), \tag{3.14}$$

with $A = 10^{-3}$ and $b = 1 \times 10^7$ cm. The size of the initial perturbation was chosen such that the main feature of the perturbation is resolved similarly well in both solvers. The solution is evolved to $t = 7.32 \times 10^{-2}$ s on $N = 128^2$. A scatter plot of the solution is shown in Figure 6. The scatter in the well-balanced scheme is significantly reduced compared to the unbalanced scheme. Unlike the unbalanced solution, the well-balanced solution remains constant ahead of the perturbation and returns to rest after the perturbation has passed.

The reference solution is computed using a one-dimensional, cylindrically symmetric, well-balanced finite volume code with a resolution of $N = 8192$.

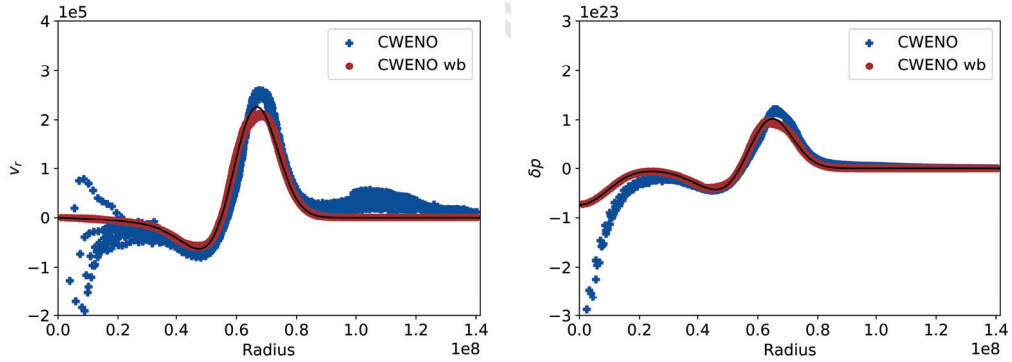

Figure 6: **Snapshots of the two-dimensional white-dwarf, see Section 3.3.2 with a small perturbation. The simulation is performed with $N = 128^2$ cells and run up to time $t = 7.32 \times 10^{-2}$ s. The radial velocity is shown on the left, the pressure perturbation on the right. The units in the plot are CGS.**

4. Conclusion

We presented a novel well-balanced, high-order finite volume scheme for Euler equations with gravity. We are able to well-balance a large class of astrophysically relevant hydrostatic equilibria without imposing the exact equilibrium apriori. Rather, we only assume some thermodynamic information about the equilibrium, e.g. constant entropy, and solve for the equilibrium in every time step. Since the equilibrium defined

by (1.6) is only a mechanical equilibrium, it seems natural that some additional information about the thermodynamic nature of the equilibrium must always be imposed.

The important features of the proposed scheme are:

- Its independence of a particular form of equation of state. This scheme can handle arbitrary equations of state including tabulated ones, as shown in the final numerical experiment.
- Its independence of a particular gravitational potential. The only requirement is that the gravitation potential and its gradient can be evaluated at apriori known locations in the computation domain. In fact the gravitation source term does not need to be constant in time. Therefore this scheme can also be applied to simulations which include self-gravity. Such simulations may benefit from well-balancing if the initial conditions are at rest and perturbed by some other means, such as a heating source term.
- Its modular nature. The scheme clearly describes how any reconstruction procedure can be made well-balanced. Therefore, the proposed scheme can be extended to arbitrary orders in a straightforward manner.
- Its local nature. The well-balancing is local to each cell. In particular it does not change the stencil required to update the cell.

The numerical experiments have shown that the scheme is high-order accurate for flows both near and far away from hydrostatic equilibrium. In fact, the numerical results suggest that the scheme is no worse on large perturbations than the equivalent unbalanced scheme. We have also shown that the schemes are stable in the presence of shocks. Furthermore, the smooth tests show that the well-balanced scheme preserves radial symmetry much better than the unbalanced scheme. Furthermore, the well-balanced solutions do not cause any changes in the part of the domain the perturbation has not reached yet. Additionally, the well-balanced scheme returns to rest after the perturbation has passed over some region in the domain, while the unbalanced scheme does neither. These tests were performed under a variety of conditions, i.e. in one dimension for constant gravity, in two dimensions for non-grid aligned gravity with both the ideal gas law and a complex multiphysics equation of state.

Our scheme only affects the reconstruction procedure and the numerical source term. Therefore, large parts of an existing finite volume code would remain unaffected by adding our well-balancing. By reusing the existing unbalanced reconstruction procedure for the perturbation the cost of implementing our scheme is further reduced. These very localized and modular changes ensure that our method can be used to well-balance a variety of existing finite volume schemes with minimal effort.

Acknowledgments

The work was supported by the Swiss National Science Foundation (SNSF) under grant 200021-169631. The authors also acknowledge the use of computational resources provided by the Swiss SuperComputing Center (CSCS), under the allocation grant s661, s665, s667 and s744. We acknowledge the computational resources provided by the EULER cluster of ETHZ.

We happily acknowledge the use of the following C++ software libraries: OpenMPI [46], HDF5 [47] and Boost. As well as the Python packages NumPy and SciPy [48], Matplotlib [49] and h5py [50].

[1] J. Greenberg, A. Leroux, A well-balanced scheme for the numerical processing of source terms in hyperbolic equations, SIAM Journal on Numerical Analysis 33 (1) (1996) 1–16. arXiv:http://epubs.siam.org/doi/pdf/10.1137/0733001, doi:10.1137/0733001.
URL http://epubs.siam.org/doi/abs/10.1137/0733001

[2] R. J. LeVeque, Balancing source terms and flux gradients in high-resolution Godunov methods: The quasi-steady wave-propagation algorithm, J. Comput. Phys. 146 (1) (1998) 346–365.
URL http://www.sciencedirect.com/science/article/B6WHY-45J58TW-22/2/72a8af8c9e23f63b0df9484475f7e2df

[3] E. Audusse, F. Bouchut, M.-O. Bristeau, R. Klein, B. Perthame, A fast and stable well-balanced scheme with hydrostatic reconstruction for shallow water flows, SIAM Journal on Scientific Computing 25 (6) (2004) 2050–2065. doi:10.1137/S1064827503431090.
URL http://link.aip.org/link/?SCE/25/2050/1

[4] S. Noelle, N. Pankratz, G. Puppo, J. R. Natvig, Well-balanced finite volume schemes of arbitrary order of accuracy for shallow water flows, J. Comput. Phys. 213 (2) (2006) 474–499. doi:10.1016/j.jcp.2005.08.019.
URL http://dx.doi.org/10.1016/j.jcp.2005.08.019

[5] L. Gosse, Computing Qualitatively Correct Approximations of Balance Laws, Springer Milan, 2013. doi:10.1007/978-88-470-2892-0.

[6] R. J. LeVeque, D. S. Bale, Wave propagation methods for conservation laws with source terms, in: Hyperbolic problems: theory, numerics, applications, Vol. II (Zürich, 1998), Vol. 130 of Internat. Ser. Numer. Math., Birkhäuser, Basel, 1999, pp. 609–618.

[7] N. Botta, R. Klein, S. Langenberg, S. Lützenkirchen, Well balanced finite volume methods for nearly hydrostatic flows, Journal of Computational Physics 196 (2) (2004) 539 – 565. doi:DOI:10.1016/j.jcp.2003.11.008.
URL http://www.sciencedirect.com/science/article/B6WHY-4B6KFKV-6/2/e4bcb5c4911970ef655c3258bd87f4c9

[8] R. J. LeVeque, A well-balanced path-integral f-wave method for hyperbolic problems with source terms, Journal of Scientific Computing 48 (2011) 209–226. doi:10.1007/s10915-010-9411-0.

[9] R. Käppeli, S. Mishra, Well-balanced schemes for the Euler equations with gravitation, Journal of Computational Physics 259 (0) (2014) 199 – 219. doi:http://dx.doi.org/10.1016/j.jcp.2013.11.028.
URL http://www.sciencedirect.com/science/article/pii/S0021999113007900

[10] V. Desveaux, M. Zenk, C. Berthon, C. Klingenberg, A well-balanced scheme for the Euler equation with a gravitational potential, Springer Proceedings in Mathematics & Statistics (2014) 217 – 226doi:10.1007/978-3-319-05684-5_20.
URL http://dx.doi.org/10.1007/978-3-319-05684-5_20

[11] P. Chandrashekar, C. Klingenberg, A second order well-balanced finite volume scheme for Euler equations with gravity, SIAM Journal on Scientific Computing 37 (3) (2015) B382–B402. arXiv:http://dx.doi.org/10.1137/140984373, doi:10.1137/140984373.
URL http://dx.doi.org/10.1137/140984373

[12] R. Käppeli, S. Mishra, A well-balanced finite volume scheme for the Euler equations with gravitation. the exact preservation of hydrostatic equilibrium with arbitrary entropy stratification, Astronomy and Astrophysics 587 (2016) A94. doi:10.1051/0004-6361/201527815.

[13] R. Touma, U. Koley, C. Klingenberg, Well-balanced unstaggered central schemes for the Euler equations with gravitation, SIAM Journal on Scientific Computing 38 (5) (2016) B773–B807. doi:10.1137/140992667.

[14] G. Li, Y. Xing, High order finite volume WENO schemes for the Euler equations under gravitational fields, Journal of Computational Physics 316 (2016) 145–163. doi:10.1016/j.jcp.2016.04.015.

[15] R. Käppeli, A well-balanced scheme for the Euler equations with gravitation, in: Innovative Algorithms and Analysis, Springer International Publishing, 2017, pp. 229–241. doi:10.1007/978-3-319-49262-9_8.

[16] A. Chertock, S. Cui, A. Kurganov, Ş. N. Özcan, E. Tadmor, Well-balanced schemes for the Euler equations with gravitation: Conservative formulation using global fluxes, Journal of Computational Physics 358 (2018) 36–52. doi:10.1016/j.jcp.2017.12.026.

[17] E. Gaburro, M. J. Castro, M. Dumbser, Well balanced Arbitrary-Lagrangian-Eulerian finite volume schemes on moving nonconforming meshes for the Euler equations of gasdynamics with gravity, Monthly Notices of the Royal Astronomical Society 477 (2) (2018) 2251 – 2275. doi:10.1093/mnras/sty542.

[18] Y. Xing, C.-W. Shu, High order well-balanced WENO scheme for the gas dynamics equations under gravitational fields, J. Sci. Comput. 54 (2-3) (2013) 645–662. doi:10.1007/s10915-012-9585-8.
URL http://dx.doi.org/10.1007/s10915-012-9585-8

[19] G. Li, Y. Xing, Well-balanced finite difference weighted essentially non-oscillatory schemes for the Euler equations with static gravitational fields, Computers & Mathematics with Applications 75 (6) (2018) 2071–2085. doi:10.1016/j.camwa.2017.10.015.

[20] G. Li, Y. Xing, Well-balanced discontinuous Galerkin methods for the Euler equations under gravitational fields, Journal of Scientific Computing (2015) 1–21doi:10.1007/s10915-015-0093-5.
URL http://dx.doi.org/10.1007/s10915-015-0093-5

[21] P. Chandrashekar, M. Zenk, Well-balanced nodal discontinuous Galerkin method for Euler equations with gravity, Journal of Scientific Computing 71 (3) (2017) 1062–1093. doi:10.1007/s10915-016-0339-x.

[22] G. Li, Y. Xing, Well-balanced discontinuous Galerkin methods with hydrostatic reconstruction for the Euler equations with gravitation, Journal of Computational Physics 352 (2018) 445–462. doi:10.1016/j.jcp.2017.09.063.

[23] F. Fuchs, A. McMurry, S. Mishra, N. Risebro, K. Waagan, High order well-balanced finite volume schemes for simulating wave propagation in stratified magnetic atmospheres, Journal of Computational Physics 229 (11) (2010) 4033 – 4058. doi:DOI:10.1016/j.jcp.2010.01.038.
URL http://www.sciencedirect.com/science/article/B6WHY-4YCWNPG-1/2/30d9ce6fa6ed0f45a553a51349bfe204

[24] C. Klingenberg, G. Puppo, M. Semplice, Arbitrary order finite volume well-balanced schemes for the Euler equations with gravity, ArXiv e-printsarXiv:1807.02341.

[25] G. K. Vallis, Atmospheric and Oceanic Fluid Dynamics, Cambridge University Press, 2006, cambridge Books Online.
URL http://dx.doi.org/10.1017/CBO9780511790447

[26] R. Kippenhahn, A. Weigert, A. Weiss, Stellar structure and evolution, Astronomy and Astrophysics Librarydoi:10.1007/978-3-642-30304-3.
URL http://dx.doi.org/10.1007/978-3-642-30304-3

[27] S. L. Shapiro, S. A. Teukolsky, Black Holes, White Dwarfs, and Neutron Stars, Wiley-VCH Verlag GmbH, 2007. doi:10.1002/9783527617661.fmatter.

[28] P. Batten, N. Clarke, C. Lambert, D. M. Causon, On the choice of wavespeeds for the hllc Riemann solver, SIAM Journal on Scientific Computing 18 (6) (1997) 1553–1570. doi:10.1137/S1064827593260140.
URL http://link.aip.org/link/?SCE/18/1553/1

[29] E. F. Toro, Riemann Solvers and Numerical Methods for Fluid Dynamics. A Practical Introduction, Springer-Verlag GmbH, 1997.

[30] B. van Leer, Towards the ultimate conservative difference scheme. V. A second-order sequel to Godunov's method, Journal of Computational Physics 32 (1) (1979) 101–136. doi:10.1016/0021-9991(79)90145-1.

[31] A. Harten, High resolution schemes for hyperbolic conservation laws, Journal of Computational Physics 49 (3) (1983) 357–393. doi:10.1016/0021-9991(83)90136-5.

[32] P. Colella, P. R. Woodward, The piecewise parabolic method (ppm) for gas-dynamical simulations, J. Comput. Phys. 54 (1) (1984) 174–201.
URL http://www.sciencedirect.com/science/article/B6WHY-4DD1PHM-SJ/2/13d69a59afba3d6a5d6bbf1144d860aa

[33] A. Harten, B. Engquist, S. Osher, S. R. Chakravarthy, Uniformly high order accurate essentially non-oscillatory schemes, III, Journal of Computational Physics 71 (2) (1987) 231–303. doi:10.1016/0021-9991(87)90031-3.

[34] C.-W. Shu, High order weighted essentially nonoscillatory schemes for convection dominated problems, SIAM Review 51 (1) (2009) 82–126. doi:10.1137/070679065.

[35] I. Cravero, G. Puppo, M. Semplice, G. Visconti, CWENO: Uniformly accurate reconstructions for balance laws, Mathematics of Computation 87 (2017) 1689–1719. doi:10.1090/mcom/3273.

[36] S. Gottlieb, C.-W. Shu, E. Tadmor, Strong stability-preserving high-order time discretization methods, SIAM Review 43 (1) (2001) 89–112. doi:10.1137/S003614450036757X.
URL http://link.aip.org/link/?SIR/43/89/1

[37] R. Courant, K. Friedrichs, H. Lewy, Über die partiellen differenzengleichungen der mathematischen physik, Mathematische Annalen 100 (1) (1928) 32–74. doi:10.1007/BF01448839.
URL https://doi.org/10.1007/BF01448839

[38] E. Godlewski, P.-A. Raviart, Numerical approximation of hyperbolic systems of conservation laws, Applied Mathematical Sciencesdoi:10.1007/978-1-4612-0713-9.
URL http://dx.doi.org/10.1007/978-1-4612-0713-9

[39] C. Hirsch, Numerical Computation of Internal and External Flows: The Fundamentals of Computational Fluid Dynamics: The Fundamentals of Computational Fluid Dynamics, Vol. 1, Butterworth-Heinemann, 2007.

[40] C. B. Laney, Computational Gasdynamics, Cambridge University Press, 1998. doi:10.1017/cbo9780511605604.
URL http://dx.doi.org/10.1017/CBO9780511605604

[41] D. Levy, G. Puppo, G. Russo, Compact Central WENO schemes for multidimensional conservation laws, SIAM Journal on Scientific Computing 22 (2) (2000) 656–672. arXiv:https://doi.org/10.1137/S1064827599359461, doi:10.1137/S1064827599359461.
URL https://doi.org/10.1137/S1064827599359461

[42] S. Chandrasekhar, An introduction to the study of stellar structure, New York: Dover, 1967.

[43] F. X. Timmes, F. D. Swesty, The accuracy, consistency, and speed of an electron-positron equation of state based on table interpolation of the Helmholtz free energy, The Astrophysical Journal Supplement Series 126 (2) (2000) 501 –516.
URL http://stacks.iop.org/0067-0049/126/i=2/a=501

[44] F. X. Timmes, http://cococubed.asu.edu/code_pages/eos.shtml (2013). [link].
URL http://cococubed.asu.edu/code_pages/eos.shtml

[45] W. H. Press, S. A. Teukolsky, W. T. Vetterling, B. P. Flannery, Numerical Recipes in FORTRAN; The Art of Scientific Computing, 2nd Edition, Cambridge University Press, New York, NY, USA, 1993.

[46] E. Gabriel, G. E. Fagg, G. Bosilca, T. Angskun, J. J. Dongarra, J. M. Squyres, V. Sahay, P. Kambadur, B. Barrett, A. Lumsdaine, R. H. Castain, D. J. Daniel, R. L. Graham, T. S. Woodall, Open MPI: Goals, concept, and design of a next generation MPI implementation, in: Proceedings, 11th European PVM/MPI Users' Group Meeting, Budapest, Hungary, 2004, pp. 97–104.

[47] The HDF Group, Hierarchical Data Format, version 5, http://www.hdfgroup.org/HDF5/ (1997-NNNN).

[48] E. Jones, T. Oliphant, P. Peterson, et al., SciPy: Open source scientific tools for Python (2001–).
URL http://www.scipy.org/

[49] J. D. Hunter, Matplotlib: A 2d graphics environment, Computing In Science & Engineering 9 (3) (2007) 90–95. doi:10.1109/MCSE.2007.55.

[50] A. Collette, Python and HDF5, O'Reilly, 2013.

Appendix A. Equilibrium reconstruction for the ideal gas law

In the ideal gas case, it can be shown that a unique equilibrium exists which matches the cell-averages, i.e. satisfies (2.13) (in one dimension) and (2.33) (in two dimensions).

In a first step the system is reduced to a single nonlinear equation in one unknown. To this end, we write the ideal gas law in the polytropic form

$$p = p(K, \rho) = K\rho^{\gamma}, \tag{A.1}$$

where $K = K(s)$ is a function of entropy s alone and γ is the ratio of specific heats. Then the equilibrium density and internal energy density can be expressed as functions of the constant $K_{0,i}$ and the enthalpy at cell center $h_{0,i}$:

$$\begin{aligned}\rho_{eq,i}(x) &= \left(\frac{1}{K_{0,i}}\frac{\gamma-1}{\gamma}h_{eq,i}(x)\right)^{\frac{1}{\gamma-1}} \\ \rho e_{eq,i}(x) &= \frac{1}{\gamma-1}\left(\frac{1}{K_{0,i}}\right)^{\frac{1}{\gamma-1}}\left(\frac{\gamma-1}{\gamma}h_{eq,i}(x)\right)^{\frac{\gamma}{\gamma-1}}.\end{aligned} \tag{A.2}$$

By plugging the latter into (2.13), one obtains a single equation for $h_{0,i}$

$$\overline{\rho e}_i = \frac{\overline{\rho}_i}{\gamma-1}\frac{\sum_{j=1}^{N_q} w_j\left(\frac{\gamma-1}{\gamma}\left(h_{0,i}+\phi_i-\phi(x_j)\right)\right)^{\frac{\gamma}{\gamma-1}}}{\sum_{j=1}^{N_q} w_j\left(\frac{\gamma-1}{\gamma}\left(h_{0,i}+\phi_i-\phi(x_j)\right)\right)^{\frac{1}{\gamma-1}}} =: f(h_{0,i}) \tag{A.3}$$

and the constant $K_{0,i}$ is simply given by

$$K_{0,i} = \left[\frac{1}{\Delta x\,\overline{\rho}_i}\sum_{j=1}^{N_q} w_j\left(\frac{\gamma-1}{\gamma}\left(h_{0,i}+\phi_i-\phi(x_j)\right)\right)^{\frac{1}{\gamma-1}}\right]^{\gamma-1}. \tag{A.4}$$

To show that (A.3) has a unique solution we show that it is monotone. Therefore, we differentiate f and find

$$f'(h_{0,i}) = \frac{\overline{\rho}_i}{\gamma-1}\left(1-\frac{1}{\gamma}\frac{\sum_{j=1}^{N_q} w_j\left(h_{0,i}+\phi_i-\phi(x_j)\right)^{\frac{\gamma}{\gamma-1}}\cdot\sum_{j=1}^{N_q} w_j\left(h_{0,i}+\phi_i-\phi(x_j)\right)^{\frac{2-\gamma}{\gamma-1}}}{\left(\sum_{j=1}^{N_q} w_j\left(h_{0,i}+\phi_i-\phi(x_j)\right)^{\frac{1}{\gamma-1}}\right)^2}\right). \tag{A.5}$$

Clearly, the second term is positive, and if it were less than γ the derivative of f would be positive, everywhere, and therefore f would be a strictly monotone function. If within every cell ϕ does not vary too much, this turns out to be true and can be proven as follows.

Let

$$h_{max,i} = h_{0,i} + \max_{x\in[x_{i-1/2},x_{i+1/2}]}\phi_i-\phi(x) \tag{A.6}$$

$$h_{min,i} = h_{0,i} + \min_{x\in[x_{i-1/2},x_{i+1/2}]}\phi_i-\phi(x) \tag{A.7}$$

then for $1<\gamma\le 2$ we find

$$\frac{\sum_{j=1}^{N_q} w_j\left(h_{0,i}+\phi_i-\phi(x_j)\right)^{\frac{\gamma}{\gamma-1}}\cdot\sum_{j=1}^{N_q} w_j\left(h_{0,i}+\phi_i-\phi(x_j)\right)^{\frac{2-\gamma}{\gamma-1}}}{\left(\sum_{j=1}^{N_q} w_j\left(h_{0,i}+\phi_i-\phi(x_j)\right)^{\frac{1}{\gamma-1}}\right)^2} \tag{A.8}$$

$$\le \frac{\sum_{j=1}^{N_q} w_j h_{max,i}^{\frac{\gamma}{\gamma-1}}\cdot\sum_{j=1}^{N_q} w_j h_{max,i}^{\frac{2-\gamma}{\gamma-1}}}{\left(\sum_{j=1}^{N_q} w_j h_{min,i}^{\frac{1}{\gamma-1}}\right)^2} = \frac{h_{max,i}^2}{h_{min,i}^2}. \tag{A.9}$$

Therefore, under the condition that

$$\frac{h_{max,i}}{h_{min,i}} < \gamma^{1/2} \tag{A.10}$$

f has a unique solution. By a very similar estimate we find that for $\gamma > 2$ a unique solution exists provided

$$\frac{h_{max,i}}{h_{min,i}} < \gamma^{\frac{\gamma-1}{\gamma}}. \tag{A.11}$$

These conditions limit the amount the gravitational potential ϕ can vary within a cell. Note that this implies a condition on the numerical resolution and puts a requirement on the cell width.